RSC Advances

Large-scale fabrication of porous carbon-decorated iron oxide microcuboids from Fe-MOFs as high-performance anode materials for lithium-ion batteries

Journal:	*RSC Advances*
Manuscript ID:	RA-ART-10-2014-011900.R1
Article Type:	Paper
Date Submitted by the Author:	23-Nov-2014

Complete List of Authors:	Li, Min-Chan; Central South University, School of Chemistry & Chemical Engineering; South University of Science and Technology of China, Department of Materials Science and Engineering Wang, Wenxi; South University of Science and Technology of China, Department of Materials Science and Engineering Yang, Mingyang; Central South University, School of Chemistry & Chemical Engineering Lv, Fucong; South University of Science and Technology of China, Department of Materials Science and Engineering Cao, Lujie; South University of Science and Technology of China, School of Chemistry & Chemical Engineering Lu, Zhouguang; South University of Science and Technology of China, Materials Science and Engineering

RSC advances

RSCPublishing

ARTICLE

Large-scale fabrication of porous carbon-decorated iron oxide microcuboids from Fe-MOF as high-performance anode materials for lithium-ion batteries

Cite this: DOI: 10.1039/x0xx00000x

Received 00th January 2012,
Accepted 00th January 2012

DOI: 10.1039/x0xx00000x

www.rsc.org/

Minchan Li,[ab] Wenxi Wang,[b] Mingyang Yang,[ab] Fucong Lv,[b] Lujie Cao[b] and Zhouguang Lu*[b]

A facile, cost effective and environmental friendly route has been developed to synthesize porous carbon-decorated iron oxides in large scale via annealing iron metal-organic framework (MOF) precursors. The as-prepared C-Fe_3O_4 particles appears in a microcuboid-like morphology that are actually assembled by ultrafine nanoparticles and exhibit greatly enhanced performance of lithium storage with high specific capacity, excellent cycling stability and good rate capability. The C-Fe_3O_4 electrodes demonstrate high reversible capacity of 975 mAh g^{-1} after 50 cycles at a current density of 100 mA g^{-1} and remarkable rate performance showing a capacity of 1124, 1042, 886 and 695 mAh g^{-1} at the current density of 100, 200, 500 and 1000 mA g^{-1}, respectively. The satisfactory electrochemical performance was contributed to the hierarchical architecture taking advantages of the synergistic effects of high conductivity of the carbon matrix, the cuboid-like secondary particles in microscale, and ultrafine primary nanoparticles in very nanoscale. Such low-cost and simple method provides the possibility to prepare anode materials in large scale, and hence may have great potential applications in energy storage and conversion.

1. Introduction

The continuously surging in crude-oil prices and aggravating global warming urge great effort to develop clean and efficient energy storage technologies. Lithium-ion batteries (LIBs), owing to their high energy density, long cycle lifespan, flexible and lightweight design, even environmental benignancy, have become promising candidate available from existing rechargeable battery techniques.[1, 2] To satisfy the ever-increasing demands for high-performance LIBs for large-scale energy applications, including electric vehicles (EV), hybrid electric vehicles (HEV) and stationary electrical energy storage, much attention has been attracted to develop advanced electrode materials with low-cost, improved safety, high energy density, along with easy synthesis and processing approaches.[3]

Graphite, the anode material currently used in commercial LIBs, has relatively low Li^+ storage capacity of 370 mAh g^{-1}. Thus, the search for alternative anode materials has become an urgent task in building the next generation LIBs, so as to meet the ever-growing performance demands.[4] Among various anode materials for LIBs, iron oxides have been proven to be appealing candidates because of their high theoretical capacities (~1000 mAh g^{-1}), wide spread availability, and environmental benignity.[5-7] Nonetheless, the rapid capacity fading which is mainly caused by the structural reorganization and volumetric variation upon charge/discharge has impeded their practical applications.[8, 9] Many efforts have been devoted to synthesizing nanostructured porous materials. It is, in fact, expected that nanomaterials accommodate the mechanical strain of Li^+ insertion/extraction much better than bulk counterparts and provide shorter path lengths for the transport of electrons and lithium ions.[7, 10-14] Meanwhile, sufficient internal porosity ensures maximum electrode stability by the large volume variation of electrode upon cycling.[15-18] However, the potential disadvantages associated with the development of nanostructured anode is the possibility of significant side-reactions with the electrolyte due to the high external surface to volume ratio and large surface free energy caused undesirable side reactions and the formation of thick solid electrolyte interphase (SEI) film, leading to safety concerns and poor calendar life.[19-21] These problems may be solved with secondary nanomaterials that the particles are typically of micrometer dimensions but internally consisting nanometer-sized regions, which could favor reducing side reactions with electrolyte leading to considerably enhanced electrochemical properties. Consequently, such proper structures provided (hollow/porous structure, suitable size, surface feature, and so on) could buffer the volume variation to sustain structural integrity and promote lithium storage reactions, which result in fast ion/electron transfer and sufficient contact between active materials and electrolyte. Improved electrode

performance such as higher overall capacity, better high-rate capability, and longer cycling life can be expected.

Metal organic frameworks (MOFs), first defined by Yaghi and co-works in 1995[22, 23] following the pioneering works of Hoskins and Robson[24-26], are crystalline porous hybrid materials comprising coupling units (metal ions or metal-oxo units) coordinated by electro-donating organic ligands. MOFs demonstrate the highest specific surface areas reported to date for porous materials and large internal pore volumes with well organized pore size.[27, 28] They have emerged as a promising class of porous materials in a wide range of extended applications, including gas storage and separation,[29] catalysis,[30] imaging and sensing.[31] Recently, a new burgeoning direction in the field of MOFs is utilized as template to synthesize hollow/porous structured inorganic nanomaterials via thermolysis. For example, by using MIL-88-Fe MOFs as templates, spindle-like mesoporous α-Fe_2O_3 has been synthesized for high-rate LIBs.[32] Hollow octahedral CuO has also been obtained by thermal treatment of Cu-based MOFs.[33] Nevertheless, to the best of our knowledge, there has been no report about the design and preparation of carbon-decorated iron oxide microcuboides from Fe-MOFs. Meanwhile, ferrous oxalate dehydrate, so-called Humboldtine in the field of mineralogy, is one of the simplest MOFs and was found in brown coal about a century ago and is also available in soil. It has one dimensional (1D) chain composed of ferrous ions and oxalate, as shown in Fig 1(a).[34, 35]

In this work, we present a simple method for the large-scale preparation of iron oxides by using $FeC_2O_4{\cdot}2H_2O$ as template to fabricate porous α-Fe_2O_3 and carbon decorated Fe_3O_4 (C-Fe_3O_4) microcuboids. Carbon coating has often been shown in recent years to improve the electrochemical performances of anode and cathode materials due to its high electronic conductivity, good lithium permeability, and electrochemical stability.[36] When evaluated as anode materials for LIBs, the as-synthesized porous carbon decorated material iron oxides exhibited excellent electrochemical performance, including a high reversible capacity and excellent rate capabilities.

2. Experimental section

2.1 Synthesis of $FeC_2O_4{\cdot}2H_2O$

Ferrous oxalate dehydrate was synthesized according to the literature.[35] Firstly, oxalic acid dihydrate (2521 mg, 20 mmol) and potassium oxalate dihydrate (3684 mg, 20 mmol) was dissolved in 180 ml deionized water with magnetic stirring. Then, ferrous oxalate heptahydrate (2780 mg, 10 mmol) was added to such a stirred solution. The mixture was kept 90 ^oC in oil bath pan for one hour. Yellow precipitate was collected by filtration, and washing with water for three times. The obtained yellow powder was dried at 50 ^oC overnight.

2.2 Synthesis of mesoporous carbon-decorated Fe_3O_4 microcuboids

In order to obtain mesoporous Fe_3O_4 carbon-decorated microcuboids, the as prepared $FeC_2O_4{\cdot}2H_2O$ microcuboids precursor was transferred into a tube furnace, and calcined at 400 ^oC for 2 hours under a flowing N_2. After cooling down, the $FeC_2O_4{\cdot}2H_2O$ microcuboids precursor changed from yellow to black, which meant that $FeC_2O_4{\cdot}2H_2O$ microcuboids have transformed into Fe_3O_4 microcuboids.

2.3 Synthesis of mesoporous α-Fe_2O_3 microcuboids

The single-crystalline mesoporous α-Fe_2O_3 microcuboids were prepared by the following procedure. Changing the atmosphere, and heated at 400 ^oC for 2 hours under air in muffle furnace. As a result, the red powers we obtained were α-Fe_2O_3 microcuboids.

2.4 Characterizations

The phase structure of samples were identified with powder X-ray diffraction (XRD) taken on a Rigaku D/Max-2400 X-ray diffractometer with Cu-Kα radiation (λ= 1.54056 Å). Raman spectra of samples were obtained on a Lab RAM HR 800 Raman microscope with an excitation laser beam wavelength of 633 nm. The morphologies and microstructures of samples were observed by scanning electron microscopy (SEM; FEI, Nova Nano SEM 450). Transmission electron microscopy (TEM) and high resolution TEM images were conducted on a Tecnai G2 F20 TEM with an accelerating voltage of 200 kV.

2.5 Electrochemical measurements

All electrochemical measurements were carried out using CR 2016 type coin cells assembled in an argon-filled glovebox (MBRAUN). The working electrode was fabricated by mixing the electroactive materials (Fe_3O_4, α-Fe_2O_3), acetylene black and polyvinylidenefluoride (PVDF) with a mass ratio of 70:20:10 in N-methyl-2-pyrrolidone (NMP) to form slurry, which was subsequently pasted on a pure Cu foil and dried at 120 ^oC in a vacuum oven overnight. A pure lithium foil was used as both the counter and reference electrodes. 1 M $LiPF_6$ in ethylene carbonate (EC)-dimethyl carbonate (DMC) (1:1 in volume) as the electrolyte. The galvanostatic charge/discharge tests of the assembled cells were carried out on an Arbin-BT2000 battery in the voltage range of 0.05–3 V at room temperature. The cyclic voltammetry (CV) measurements were performed at the same voltage window at a scan rate of 0.1 mV/s on a BioLogic-VMP3 electrochemical workstation. EIS were also recorded on the electrochemical workstation with the frequency ranging from 100 mHz to 100 kHz at room temperature.

3. Results and discussion

3.1 Structure and Morphology

Figure.1 shows the XRD pattern of the precursor and the products after calcination. In Fig. 1(b-1) all the diffraction peaks can be indexed to $FeC_2O_4{\cdot}2H2O$ (JCPDS no.72-1305). No other impurity peaks are observed, and the strong and sharp diffraction peaks indicate the highly crystalline nature. After calcining the iron oxalate precursor in air and inert atmosphere, phase-pure α-Fe_2O_3 (JCPDS no.33-0664) and Fe_3O_4 (JCPDS no.19-0629) are obtained as shown in Fig. 1(b-2) and (b-3), respectively.

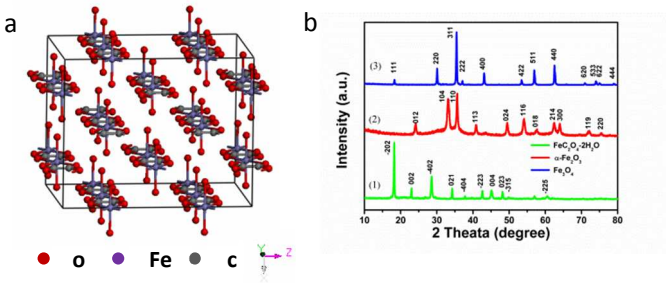

Figure 1. (a). crystal structure of ferrous oxalate dehydrate. (b). XRD patterns of (1) $FeC_2O_4 \cdot 2H_2O$, (2) α-Fe_2O_3, and (3) Fe_3O_4

The obtained Fe_3O_4 products are further analysed by Raman spectroscopy as presented in Figure 2a. It shows the characteristic peaks of magnetite at 331, 532 and 661 cm^{-1} that can be assigned to the E_g, T_g and A_{1g} vibration modes of Fe-O,[37] respectively, confirming that the as-synthesized products are composed of single phase of magnetite Fe_3O_4. Meanwhile, two distinguishable peaks can be observed at about 1348 cm^{-1} and 1590 cm^{-1}, which can be ascribed to the D-band and G-band of carbon, respectively. The D-band is associated with disorder coordination of carbon, allowing zone edge modes of the graphite structure to become active due to the lack of long-range order in amorphous and quasi-crystalline forms of residual carbon in the C-Fe_3O_4 composites. The G-band corresponds to the E_{2g} stretching vibrations in the basal plane of the ordered crystalline graphite. The peak intensity ratio between D- and G-bands (I_D/I_G) provides a useful index for comparing the degree of crystallinity of various carbon materials, that is, the smaller the ratio of I_D/I_G, the higher the degree of ordering in the carbon composition.[20, 38] The I_D/I_G ratio for C-Fe_3O_4 microcuboids is calculated to be 1.03, demonstrating that the carbon formed is not very well ordered as compared with the literatures.[37] Meanwhile, the existence of carbon matrix will be beneficial for achieving better electronic conductivity. Thermogravimetric analysis (TGA), carried out in oxygen at a heating rate of 10 ^oC min^{-1}, is used to determine the content of carbon (Figure 2b). The sample is heated to 800 ^oC so that the Fe_3O_4 is oxidized to Fe_2O_3 and the carbon is oxidized to CO_2. According to the remaining weight, the content of carbon is around 1.6 wt%.

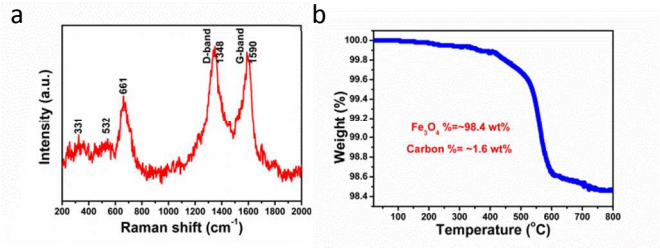

Figure 2. (a) Raman spectra of as-prepared C-Fe_3O_4. (b) TGA profile of C-Fe_3O_4.

The morphologies and microstructure of the $FeC_2O_4 \cdot 2H_2O$ precursor, and the α-Fe_2O_3 and C-Fe_3O_4 products derived from the pyrolysis of the Fe-MOFs are investigated by SEM and TEM as show in Figure 3 and Figure 4. The representative SEM images of the products shown in Fig.3 reveal uniform microcubid-like morphology with the average diameter of about 5 μm and the length of about 30 μm. Moreover, the surface of the precursor $FeC_2O_4 \cdot 2H_2O$ microcuboids appeals smooth (Fig. 3d). After annealed in air and N_2 at 400 ^oC for 2h, the microcuboids morphology are maintained, while the surface become much rougher (Fig. 3e and f). Meanwhile, the superficial cracks are developed in the restricted direction and porous structures are generated from the gas molecules releasing. The only difference is that α-Fe_2O_3 microcuboids still aggregate together, while the C-Fe_3O_4 microcuboids separate to each other. It can be clearly identified from the corresponding TEM image of Fig. 4a that the precursor $FeC_2O_4 \cdot 2H_2O$ microcubids are actually assembled from nanoplates with size of about 50-100 nm. The TEM image in Fig. 4b indicates that the α-Fe_2O_3 microcuboids are composed of porous nanoplates, which in turn consisted of ultrafine nanoparticles with size of less than 10 nm. The TEM image in Fig.4c reveals that the C-Fe_3O_4 microcuboids obtained in insert atmosphere are actually assembles consisting of ultrafine nanoparticles with size about 20 nm linked together by carbon matrix. Fig. 4d~f show the high resolution TEM images and the corresponding SAED patterns of the $FeC_2O_4 \cdot 2H_2O$ and iron oxides. Lattice fringes are clearly visible with spacing of 0.30 nm in Fig. 4d, which is in accordance with the (-402) planes of $FeC_2O_4 \cdot 2H_2O$. The crystallinity of α-Fe_2O_3 is poor, while the SAED pattern shown in inset of Fig. 4e display distinct diffraction rings that can be ascribed to the (110) and (220) of α-Fe_2O_3. The clear lattice fringes with spacing of 0.29 nm and 0.25 nm, as well as the corresponding SAED images in Fig.4f indicated that the obtained C-Fe_3O_4 particles are well-crystallized. Furthermore, it clearly shows the amorphous carbon coating on the surface of the highly crystalline Fe_3O_4, which are quite consistent with the aforementioned Raman results.

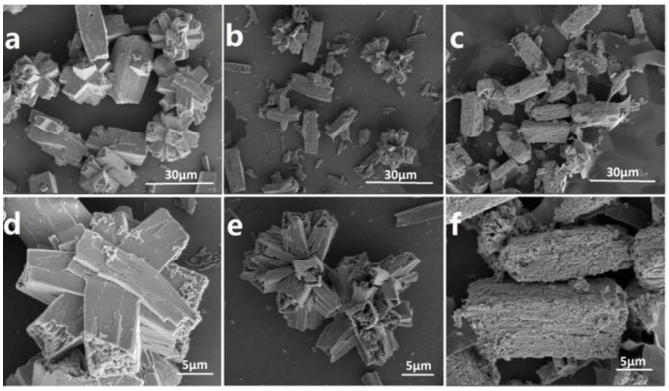

Figure 3. SEM images of as-prepared samples. (a, d) $FeC_2O_4 \cdot 2H_2O$; (b, e) α-Fe_2O_3; (c, f) Fe_3O_4.

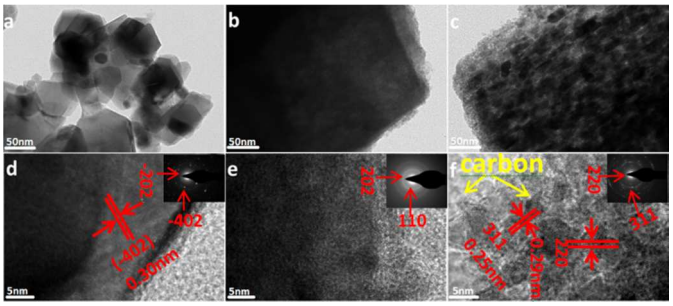

Figure 4. TEM and HRTEM images of as-prepared samples. (a, d) $FeC_2O_4 \cdot 2H_2O$; (b, e) α-Fe_2O_3; (c, f) Fe_3O_4. The insets of (d, e, f) show the corresponding SAED patterns.

3.2 Electrochemical Performance

Figure 5a shows the first three cyclic voltammogram (CV) curves of the C-Fe_3O_4 microcuboids at room temperature between 0.05 and 3.0 V at a scan rate of 0.1 mV/s. It is apparent that the CV curve of the first cycle is quite different from those of subsequent cycles, especially for the discharge branch. There are two well-defined peaks observed at 0.86 and 0.67 V (vs. Li^+/Li) in the first cathodic sweep, which indicates two steps of the lithiation reactions of C-Fe_3O_4 (step 1, $Fe_3O_4 + 2Li^+ + 2e^- \rightarrow Li_2(Fe_3O_4)$; and step 2, $Li_2(Fe_3O_4) + 6Li^+ + 6e^- \rightarrow 3Fe + 4Li_2O$)[39-41], as well as the

occurrence of side reactions on the electrode surface with electrolyte. Meanwhile, two peaks are observed at approximately 1.66 and 1.85V in anodic process, attributed to the oxidation of Fe to Fe^{2+} and Fe^{3+}, respectively. During the following two cycles, the peak intensity drops significantly, indicating the occurrence of some irreversible reactions via the formation of SEI film. It is noteworthy that, after the first cycle, the CV curves almost overlapped, which indicates that a stable SEI film was formed and a good electrochemical reversibility of the mesoporous C-Fe_3O_4.

The detailed electrochemical behavior of the α-Fe_2O_3 microcuboids is evaluated by CV tests as shown in Fig. 5b. A spiky peak is observed at 0.71 V with two small peaks appearing at 1.08 V and 1.65 V indicating the following three lithiation steps: α-Fe_2O_3 + $xLi^+ + xe^- \rightarrow$ α-$Li_xFe_2O_3$; α-$Li_xFe_2O_3$ + (2-x) $Li^+ \rightarrow Li_2Fe_2O_3$ (cubic); $Li_2Fe_2O_3$ (cubic) + $4Li^+ + 4e^- \rightarrow 2Fe + 3Li_2O$. Firstly, at the initial stage of lithium intercalation, a small amount of lithium can be inserted into the crystal structure of α-Fe_2O_3 to form hexagonal α-$Li_xFe_2O_3$, followed by a transformation to cubic $Li_2Fe_2O_3$.[42-45] The sharp peak corresponds to the reduction of iron from Fe^{2+} to Fe^0 completely and the decomposition of electrolyte. In the anodic process, on the other hand, two broad peaks are recorded at about 1.66 V and 1.91 V, corresponding to the oxidation of Fe to Fe^{2+} and further oxidization to Fe^{3+}. The subsequent cycles are significantly different from that of the first cycle as only cathodic peak appears with decreased peak intensity owning to an irreversible phase transformation from hexagonal α-$Li_xFe_2O_3$ to cubic $Li_2Fe_2O_3$ and SEI film formation.

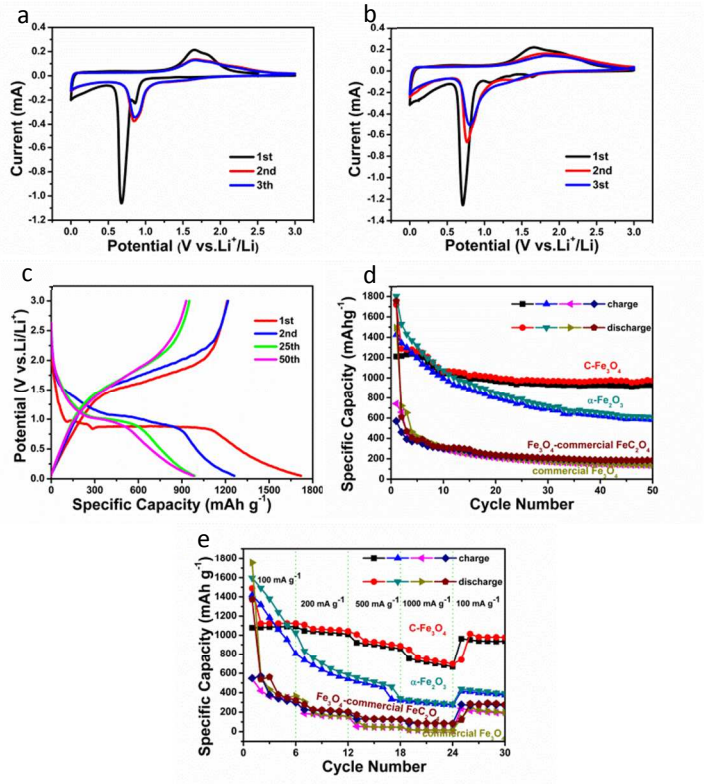

Figure 5. Electrochemical performance of the C-Fe_3O_4, α-Fe_2O_3, commercial Fe_3O_4 nanoparticles and Fe_3O_4 derived from commercial FeC_2O_4 (a, b) CV curves of (a) C-Fe_3O_4 and (b) α-Fe_2O_3 at a voltage range of 0.05 to 3.0 V (vs Li^+/Li) with a scan rate of 0.1 mV s^{-1}. (c) Voltage profiles plotted for the 1st, 2nd, 25th, 50th cycles of the C-Fe_3O_4 electrode at a current density of 100 mAh g^{-1}. (d) Cycle performance of all samples at a current density of 100 mAh g^{-1}. (e) Comparison of the rate capabilities of all samples at various current densities between 100 mAh g^{-1} and 1000 mAh g^{-1}.

Fig. 5c shows representative discharge/charge voltage profiles of C-Fe_3O_4 microcuboids at a current density of 100 mA g^{-1} between 0.05 and 3.0 V. It can be seen that the sample delivers a very high lithium storage capacity of 1719 mAh g^{-1} during the initial discharge process, but a relative low reversible capacity of 1212 mAh g^{-1} is achieved, leading to an initial Coulombic efficiency of around 70%. The relative low initial Coulombic efficiency may be caused by the irreversible capacity loss, including inevitable formation of SEI and decomposition of electrolyte, which are common to the most anode materials.[39-44] In the second cycle, however, the Coulombic efficiency increases rapidly to 94%. The discharge and charge capacities of the 2nd cycle are 1212 and 1286 mAh g^{-1}, respectively. Even after the 50th cycle, the discharge capacity of the C-Fe_3O_4 microcuboids is still maintained 975 mAh g^{-1} and the Coulombic efficiency steadily reaches around 95%, which further indicates that the C-Fe_3O_4 are extraordinary stable during cycle.

To explore the merits of the as-synthesized iron oxide microcuboids for anode materials of LIBs, we test the cycle performance of the products at 100 mA g^{-1}. For comparision, commercial Fe_3O_4 nanoparticles together with the Fe_3O_4 products derived from commercial FeC_2O_4 are also investigated under the same conditions. All results are complied in Fig. 5d. Apparently, the as prepared C-Fe_3O_4 electrode demonstrates a much better cycle retention and a much higher reversible capacity of 975 mAh g^{-1} than other samples after 50 cycles. Compared to the C-Fe_3O_4 microcuboids, the commercial Fe_3O_4 particles and Fe_3O_4 derived from commercial FeC_2O_4 quickly lose their activity in first few cycles, a significant lower capacity are delivered at the end of the 50 cycles. For the bare α-Fe_2O_3, though a capacity of 608 mAh g^{-1} is observed after 50 cycles, it still shows poor cycle performance. This evidently proves that the remarkable positive effect of the unique structure of C-Fe_3O_4 from Fe-MOFs. For the C-Fe_3O_4 microcuboids, the carbon coating has been proved to considerably improve the electrochemical performance of anode materials due to its high conductivity, good lithium permeability, and flexibility to hold the structure respectability. It is well know that the lithium storage capability of Fe_3O_4 is mainly achieved through the reversible conversion reaction between the lithium ion and Fe_3O_4, forming Fe nanocrystals well dispersed in Li_2O matrix, and the carbon shell can prevent the formed Fe nanocrystals from catalyzing the decomposition of the outer SEI. This in turn allows for the growth of a stable SEI on the surface of the carbon shell and prevents the continuous assessment rupturing and re-forming of the SEI. After the formation of a stable SEI, their capacity is maintained very well and thus the anode of C-Fe_3O_4 microcuboids exhibits exceedingly excellent cycling performance.[20, 46] However, in the bare of α-Fe_2O_3 and the commercial Fe_3O_4 nanoparticles, the SEI will rupture due to the mechanical strain generated by the volume expansion/contraction during the lithium extraction process, and thus the electrode surface would be cyclically exposed to the electrolyte. The cyclical rupture and growth of SEI can cause low Coulombic efficiency, higher resistance to ionic transport, and low electronic conductivity of the whole electrode. As to the Fe_3O_4 products derived from commercial FeC_2O_4, it still lacks of the unique structure derived from the synthesis of Fe-MOFs. Therefore, the capacity deceased rapidly, and their cycle performance is much worse than that of C-Fe_3O_4 composites.[47]

As expected, the C-Fe_3O_4 composites exhibit excellent rate capability, as displayed in Fig. 5e. When the current density is increased from 100 mA g^{-1} to 1000 mA g^{-1}, the C-Fe_3O_4 displays simultaneously promising specific capacities and rate capabilities. The discharge and charge capacities remain stable and decrease

regularly with an increased rate. The reversible capacities at 100, 200, 500 and 1000 mA g^{-1} are about 1124, 1042, 886 and 695 mAh g^{-1}. Moreover, when the current rate is finally returned to its initial value of 100 mA g^{-1}, a capacity of 976 mAh g^{-1} is still retained. It clearly demonstrates that the unique mesoporous structure combined with the carbon framework of the C-Fe_3O_4 microcuboids play important roles in relieving the impact of volume changes during the repeated charge–discharge processes, which is in good agreement with the previous reports.[20, 36, 46] Thus, these C-Fe_3O_4 microcuboids present remarkable cyclic stability and rate performance.

The electrochemical impedance spectra, a promising tool for investigating electron and ion diffusion, is conducted at the frequency ranging from 100 kHz to 100 mHz to investigate the charge transfer and Li^+ diffusion kinetics of various electrode materials. Figure 5d shows the Nyquist plots for the C-Fe_3O_4, α-Fe_2O_3, commercial Fe_3O_4 nanoparticles and Fe_3O_4 products derived from commercial FeC_2O_4 at fresh coin cells, which share the common feature of a high-frequency depressed semicircle and a medium-frequency depressed semicircle followed by a linear tail in the low frequency region. Following are the common equivalent circuit descriptions of these features: the intercept on the Z' axis at the high-frequency end is the electrolyte resistance (Rs); R_f and CPE1 are resistance and capacitance of the solid-state interface layer formed on the surface of the electrodes, which is correspond to the semicircle at high frequencies; Rct and CPE2 are faradic charge-transfer resistance and its relative double-layer capacitance, which correspond to the semicircle at medium frequencies. And the inclined line at the low-frequency region represents the Warburg impedance (Zw) related to a combination of the diffusional effects of lithium ion on the interface between the active material particles and the electrolyte. The low Rct is beneficial to enhance the electron kinetics in the electrode materials.[48, 49] Apparently, the diameter of the semicircle for C-Fe_3O_4 electrode is significantly smaller than other samples., indicating that C-Fe_3O_4 composite electrodes possess lowest contact and charge-transfer impedances, which can lead to rapid electron transport during the electrochemical lithium insertion/extraction reaction and thus result in significant improvement on the rate performance.

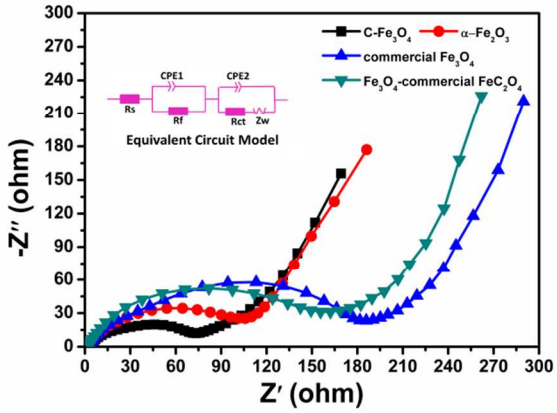

Figure 6. EIS spectra of all samples fresh cells in the frequency range from 100 mHz to 100 kHz. The inset is an equivalent circuit model.

Based on the above characterization results and electrochemical investigations, the C-Fe_3O_4 composite electrode displays extremely satisfactory electrochemical performance and structural stability. These outstanding properties can be attributed to their distinct structure and morphology that offer the following benefits: (1) the C-Fe_3O_4 microcuboids with mesoporous structures enhance the contact area between the electrode and electrolyte and allow better penetration of the electrolyte, the porous structure may ensure the short transport path for both electrons and lithium ions, leading to good conductivity and fast charge/discharge rates. (2) the carbon framework and its intimate contact with the Fe_3O_4 particles could not only provide more reactive sites on the surface, but also acts as a very efficient conducting network to facilitate the fast charge transfer and shorten the diffusion paths for the rapid Li^+ insertion/extraction. It is worth pointing out that the as-prepared C-Fe_3O_4 exhibits highly enhanced electrochemical performance over the related reports, demonstrating that the enhancement of electrochemical performance is mainly attributed to the special structure. Therefore, the strategy may pave a new path for the development of anode materials.

4. Conclusions

In summary, porous carbon-decorated iron oxides have been successfully synthesized by an exceedingly simple strategy, which involves the preparation of ferrous oxalate dehydrate as template via a facile method and subsequent thermal decomposition of the precursors at 400 ^oC in inert gas atmosphere. When tested as the anode materials for LIBs, the as-synthesized mesoporous C-Fe_3O_4 which is calcined in N_2 showed much better electrochemical performance than α-Fe2O3 in air and commercial Fe_3O_4 nanoparticles and Fe_3O_4 products derived from commercial FeC_2O_4. The large void space provided by porous structure in between the constituent Fe_3O_4 nanoparticles was desirable to mitigate the volume charge problem during the Li^+ insertion/extraction process. The residual carbon network not only facilitates the formation of a stable SEI layer on the electrode surface, but also enhances the electrode kinetics through conductivity improvements. In view of these unique structure advantages, the as-synthesized C-Fe_3O_4 evaluated as electrode exhibits excellent performance in LIBs with very stable cycling behavior and good rate capability. The low-cost and convenient method in this work can be used for large scale products and extended to the fabrication of other metal oxide with well-definite structures that may have potential applications in energy storage and conversion.

Acknowledgements

This work was supported by the National Natural Science Foundation of China (21001117) and the Starting-Up Funds of South University of Science and Technology of China (SUSTC) through the talent plan of the Shenzhen Government.

Notes and references

[a] Key Laboratory of Resource Chemistry of Nonferrous Metals, Ministry of Education, School of Chemistry & Chemical Engineering, Central South University, Changsha, Hunan 410083, China.

[b] Department of Materials Science and Engineering, South University of Science and Technology of China, Shenzhen, Guangdong 518055, China. E-mail: luzg@sustc.edu.cn

1. P. G. Bruce, B. Scrosati and J. M. Tarascon, *Angewandte Chemie International Edition*, 2008, **47**, 2930-2946.
2. M. Armand and J.-M. Tarascon, *Nature*, 2008, **451**, 652-657.
3. A. Manthiram, *The Journal of Physical Chemistry Letters*, 2011, **2**, 176-184.

4. J. S. Chen, L. A. Archer and X. W. D. Lou, *Journal of Materials Chemistry*, 2011, **21**, 9912-9924.
5. P. Poizot, S. Laruelle, S. Grugeon, L. Dupont and J. Tarascon, *Nature*, 2000, **407**, 496-499.
6. J. Cabana, L. Monconduit, D. Larcher and M. R. Palacin, *Advanced Materials*, 2010, **22**, E170-E192.
7. F. Cheng, Z. Tao, J. Liang and J. Chen, *Chemistry of Materials*, 2007, **20**, 667-681.
8. C. Li and X. D. Lou, *Chemical communications*, 2011, **47**, 8061-8063.
9. S. Jin, H. Deng, D. Long, X. Liu, L. Zhan, X. Liang, W. Qiao and L. Ling, *Journal of Power Sources*, 2011, **196**, 3887-3893.
10. X. W. Lou, Y. Wang, C. Yuan, J. Y. Lee and L. A. Archer, *Advanced Materials*, 2006, **18**, 2325-2329.
11. F. Jiao and P. G. Bruce, *Advanced Materials*, 2007, **19**, 657-660.
12. S. Grugeon, S. Laruelle, R. Herrera-Urbina, L. Dupont, P. Poizot and J. Tarascon, *Journal of The Electrochemical Society*, 2001, **148**, A285-A292.
13. J. Maier, *Nature materials*, 2005, **4**, 805-815.
14. A. M. Cao, J. S. Hu, H. P. Liang and L. J. Wan, *Angewandte Chemie International Edition*, 2005, **44**, 4391-4395.
15. R. Demir-Cakan, Y.-S. Hu, M. Antonietti, J. Maier and M.-M. Titirici, *Chemistry of Materials*, 2008, **20**, 1227-1229.
16. D. Deng and J. Y. Lee, *Chemistry of Materials*, 2008, **20**, 1841-1846.
17. F. Liu and D. Xue, *Nanoscience and Nanotechnology Letters*, 2011, **3**, 389-393.
18. J. Liu, H. Xia, L. Lu and D. Xue, *Journal of Materials Chemistry*, 2010, **20**, 1506-1510.
19. L. Hu and Q. Chen, *Nanoscale*, 2014, **6**, 1236-1257.
20. C. He, S. Wu, N. Zhao, C. Shi, E. Liu and J. Li, *ACS nano*, 2013, **7**, 4459-4469.
21. O. Delmer, P. Balaya, L. Kienle and J. Maier, *Advanced Materials*, 2008, **20**, 501-505.
22. O. Yaghi and H. Li, *Journal of the American Chemical Society*, 1995, **117**, 10401-10402.
23. O. M. Yaghi, G. Li and H. Li, *Nature*, 1995, **378**, 703-706.
24. B. F. Hoskins and R. Robson, *Journal of the American Chemical Society*, 1989, **111**, 5962-5964.
25. B. Hoskins and R. Robson, *Journal of the American Chemical Society*, 1990, **112**, 1546-1554.
26. B. Abrahams, B. Hoskins, D. Michail and R. Robson, *Nature*, 1994, **369**, 727-729.
27. H. Furukawa, N. Ko, Y. B. Go, N. Aratani, S. B. Choi, E. Choi, A. Ö. Yazaydin, R. Q. Snurr, M. O'Keeffe and J. Kim, *Science*, 2010, **329**, 424-428.
28. W. Xuan, C. Zhu, Y. Liu and Y. Cui, *Chemical Society reviews*, 2012, **41**, 1677-1695.
29. A. U. Czaja, N. Trukhan and U. Müller, *Chemical Society reviews*, 2009, **38**, 1284-1293.
30. A. Corma, H. Garcia and F. Llabrés i Xamena, *Chemical Reviews*, 2010, **110**, 4606-4655.
31. P. Horcajada, T. Chalati, C. Serre, B. Gillet, C. Sebrie, T. Baati, J. F. Eubank, D. Heurtaux, P. Clayette and C. Kreuz, *Nature materials*, 2010, **9**, 172-178.
32. X. Xu, R. Cao, S. Jeong and J. Cho, *Nano letters*, 2012, **12**, 4988-4991.
33. R. Wu, X. Qian, F. Yu, H. Liu, K. Zhou, J. Wei and Y. Huang, *Journal of Materials Chemistry A*, 2013, **1**, 11126-11129.
34. K. Rane, A. Nikumbh and A. Mukhedkar, *Journal of Materials Science*, 1981, **16**, 2387-2397.
35. T. Yamada, M. Sadakiyo and H. Kitagawa, *Journal of the American Chemical Society*, 2009, **131**, 3144-3145.
36. T. Muraliganth, A. V. Murugan and A. Manthiram, *Chemical communications*, 2009, 7360-7362.
37. O. N. Shebanova and P. Lazor, *Journal of Solid State Chemistry*, 2003, **174**, 424-430.
38. S. Urbonaite, L. Hälldahl and G. Svensson, *Carbon*, 2008, **46**, 1942-1947.
39. Z. Xiao, Y. Xia, Z. Ren, Z. Liu, G. Xu, C. Chao, X. Li, G. Shen and G. Han, *Journal of Materials Chemistry*, 2012, **22**, 20566-20573.
40. G. Zhou, D.-W. Wang, F. Li, L. Zhang, N. Li, Z.-S. Wu, L. Wen, G. Q. Lu and H.-M. Cheng, *Chemistry of Materials*, 2010, **22**, 5306-5313.
41. T. Zhu, J. S. Chen and X. W. Lou, *The Journal of Physical Chemistry C*, 2011, **115**, 9814-9820.
42. Z. Wang, Z. Wang, W. Liu, W. Xiao and X. W. D. Lou, *Energy & Environmental Science*, 2013, **6**, 87-91.
43. W. Zhou, L. Lin, W. Wang, L. Zhang, Q. Wu, J. Li and L. Guo, *The Journal of Physical Chemistry C*, 2011, **115**, 7126-7133.
44. D. Su, H.-S. Kim, W.-S. Kim and G. Wang, *Microporous and Mesoporous Materials*, 2012, **149**, 36-45.
45. S. Yuan, Z. Zhou and G. Li, *CrystEngComm*, 2011, **13**, 4709-4713.
46. J. E. Lee, S.-H. Yu, D. J. Lee, D.-C. Lee, S. I. Han, Y.-E. Sung and T. Hyeon, *Energy & Environmental Science*, 2012, **5**, 9528-9533.
47. Y. G. Guo, J. S. Hu and L. J. Wan, *Advanced Materials*, 2008, **20**, 2878-2887.
48. J. Z. Wang, C. Zhong, D. Wexler, N. H. Idris, Z. X. Wang, L. Q. Chen and H. K. Liu, *Chemistry-A European Journal*, 2011, **17**, 661-667.
49. L. Cui, J. Shen, F. Cheng, Z. Tao and J. Chen, *Journal of Power Sources*, 2011, **196**, 2195-2201.

